Materials Advances

ROYAL SOCIETY OF CHEMISTRY

PAPER

View Article Online
View Journal | View Issue



Cite this: *Mater. Adv.*, 2022, 3, 8288

# Mesoporous β-$Ag_2MoO_4$ nanopotatoes as supercapacitor electrodes†

J. Johnson William,[a] Saravanakumar Balakrishnan,[ac] Mariyappan Murugesan,[a] Muralidharan Gopalan,[b] Allen J. Britten[c] and Martin Mkandawire *[c]

Received 18th June 2022,
Accepted 14th September 2022

DOI: 10.1039/d2ma00708h

rsc.li/materials-advances

A growing quest for supercapacitors capable of quickly transferring energy has led to investigations focusing on developing electrode materials that incorporate noble metals due to their superior electrical conductivity. Here, we report the synthesis and charge storage performance of mesoporous silver molybdate electrodes of cubic β-$Ag_2MoO_4$ morphology and potatoes-like nanostructures. The electrochemical performance of the mesoporous β-$Ag_2MoO_4$ electrode has a battery-type behaviour with the transfer of two electrons ($Ag^0 \leftrightarrow Ag^{2+}$) during the redox reaction in 2 M KOH aqueous solution within a potential range of −0.45 to 0.35 V. In addition, the electrodes demonstrate quasi-conversion reaction during the discharge, which is due to the oxidation of unoxidized $Ag^0$. Furthermore, the electrodes exhibit a maximum specific capacity of 2610 C $g^{-1}$ at 1 A $g^{-1}$ and significant retention of 82% upon 5000 continuous galvanostatic charge/discharge (GCD) cycles. A battery-type asymmetric supercapacitor cell (BASC) was designed using β-$Ag_2MoO_4$ as the positive electrode, activated carbon as the negative electrode, and polyurethane foam/KOH as the separator-cum-charge reservoir. The fabricated BASCs yielded maximum specific energy of 54 W h $kg^{-1}$ at a specific power of 194 W $kg^{-1}$. These appreciable electrochemical features suggest that β-$Ag_2MoO_4$ can be a viable material for developing supercapacitor electrodes.



## Introduction

The urge for high power and energy in applications such as hybrid electric cars, electronics, and optoelectronics has necessitated the quest for developing energy storage devices that can charge and discharge at very fast rates.[1,2] One potentially trending device is supercapacitors (SCs), which have excellent properties like fast electrochemical kinetics in the charging-discharging process, long lifespan, easy operation, greater specific power and high energy.[3–5] Specifically, SCs can recover stored energy at a short interval of time, which is required in application in heavy-duty systems.[6] One of the key components to achieving outstanding charge storage performance in any energy storage device is electrode materials (both positive and negative).[7,8] Excellent electrode materials for energy storage devices are electroactive with efficient surface architectures, compatible electrochemical interaction with electrolyte, allowing binder-free fabrication of electrodes, high specific surface area, strong adherence to a current collector, and a good degree of porosity that facilitates the electron transport kinetics. As a result, a lot of research efforts have been directed to identify the materials, specifically for the negative electrodes, with the qualities mentioned above. For supercapacitors, more and more attention is being given to metal oxides with distinctive nanostructures for possible electrode material. Nanostructure metal oxides have unique charge storage capability, storing in alkaline solutions other than the rectangular double layer process through the Nernstian reaction. Furthermore, binary metal oxides make material for supercapacitors due to their multiple redox states.[9]

Among inorganic material families, metal molybdates ($A_xMoO_y$; where A site might be a mono-, di-, or trivalent metal ion)[10,11] are attracting research interest for their suitability as supercapacitor electrodes. The $A_xMoO_y$ have the right characteristics sought in electrodes like high theoretical charge capacity, good electrical and ionic conductivity and excellent electrochemical activity.[6,12,13] Although the molybdenum ions can undergo multiple redox states ($Mo^{3+}$ to $Mo^{6+}$), metal or transition metal molybdates offer a substantial degree of chemical stability against continuous charge–discharge cycles, owing to the covalent bonding in molybdates.[10,14] Additionally, these $A_xMoO_y$ have good ionic conductivity with regard to the

[a] Department of Physics, Dr. Mahalingam College of Engineering and Technology, Pollachi, 642003, India
[b] Department of Physics, The Gandhigram Rural Institute (DTBU), Gandhigram, 624302, India
[c] Department of Chemistry, Cape Breton University, 1250 Grand Lake Rd., Sydney, Nova Scotia, B1P 6L2, Canada. E-mail: martin_mkandawire@cbu.ca

† Electronic supplementary information (ESI) available. See DOI: https://doi.org/10.1039/d2ma00708h

electrolyte ions, which is responsible for the substantially high specific capacity and energy density because the conductive channels are paved with metal or transition metal ions.[4,7] Motivated by these qualities, various transition metal molybdates, including $NiMoO_4$,[15,16] $CoMoO_4$,[2,17,18] $MnMoO_4$,[19,20] $CuMoO_4$, $FeMoO_4$,[21] $Ag_2MoO_4$, $ZnMoO_4$,[22,23] $Bi_2MoO_6$,[24] $Cu_3Mo_2O_9$[25,26] and their possible composites consisting metal compounds,[27] carbon and conducting polymers have been explored for use as electrodes in supercapacitors.[28–31] For example, exploration of $MnMoO_4$ nanostructures for supercapacitor electrodes revealed an outstanding supercapacitive performance, with an estimated specific capacitance of 697.4 F $g^{-1}$ at 0.5 A $g^{-1}$ in 2 M KOH aqueous solution.[32] Similarly, $Bi_2MoO_6$ nanoplates have a good charge storage performance, accounting for a specific capacitance of 698 F $g^{-1}$ at 5 mV $s^{-1}$.[33]

Besides the high power sought for electronic devices, electrodes of the gadgets must support faster electron passage. Thus, $A_xMoO_y$ materials containing $Ag^+$ rank high in research interest because Ag has excellent electrical conductivity, attributed to the materialized $Ag^+$ (reduced product) containing an anatomically distributed network of conductive $Ag^0$ particles that facilitate rapid electron transport.[34] There are several feasible structures of $A_xMoO_y$ in the $Ag_2O$–$MoO_3$ phase diagram, including layered $Ag_6Mo_{10}O_{33}$, $Ag_2Mo_2O_7$ with its two polymorphs, orthorhombic $Ag_2Mo_3O_{10}$ and spinel $Ag_2MoO_4$.[34] However, only a few of these $Ag^+$ containing $A_xMoO_y$ have been examined, to the best of our knowledge, for their suitability and performance in supercapacitors. So far, a literature search only revealed a work that reported the coexistence of surface and intercalation redox reactions for layered-structured triclinic $Ag_6Mo_{10}O_{33}$ electrodes in energy storage.[10]

In this paper, we report a study on the development of spinel β-$Ag_2MoO_4$ nanostructures with excellent electrochemical behaviour suitable for high-performing supercapacitors. $Ag_2MoO_4$ nanostructures may be found in two polymorphic states: metastable α-$Ag_2MoO_4$ (tetragonal) and stable β-$Ag_2MoO_4$ (cubic). The β-$Ag_2MoO_4$ is of higher interest due to, among others, possessing a good range of optical gap (3.26–3.41 eV), having a spinel-type cubic structure and ease of synthesis. These attractive features make β-$Ag_2MoO_4$ a functional material for semiconductor, photo catalyst and energy storage applications. In contrast, α-$Ag_2MoO_4$ is mostly reported at high temperatures or with large amounts of surfactants.[32–34] However, the synthesis of α-$Ag_2MoO_4$ generally required extreme conditions, such as high pressure and temperature, as well as high-tech equipment. When heated above the ambient temperature, the α-phase irreversibly changes into the β-phase. The β-$Ag_2MoO_4$ phase comprises tetrahedral [$MoO_4$] clusters created by the coordination of $Mo^{6+}$ with four $O^{2-}$ anions and octahedral [$AgO_6$] clusters formed by the coordination of $Ag^+$ cations with six $O^{2-}$ anions.[35] In view of these, the electrochemical performance of β phase, cubic $Ag_2MoO_4$ nanostructures were studied. Furthermore, the β-$Ag_2MoO_4$ nanostructure is used to construct battery-type asymmetric supercapacitor cells, and the real-life application of the designed cell was investigated in the current work. The supercapacitor cells were able to energize LEDs.

## Results and discussion

### Structural, morphological and surface area analysis

The prepared materials' crystal structure, phase and purity were analyzed using X-ray diffraction spectrometry, and the results are presented in Fig. 1a. The sharp and intense diffraction peaks in Fig. 1a signify the formation of the crystalline silver molybdate. The Bragg's peaks are located at 2$\theta$ values of 16.4°, 27.1°, 31.8°, 33.2°, 38.6°, 42.2°, 47.8°, 50.9°, 55.7°, 63.1°, 65.6°, 66.5°, 76.4° and 78.8° agree with the respective reflection planes of cubic β-$Ag_2MoO_4$ (JCPDS: 08-0473).[36] No other peaks related to metallic Ag, AgO, $Ag_2O$, $Ag_3O_4$ or $MoO_3$ phase were observed, indicating that the silver molybdate crystals were of the highest purity. Further FTIR spectroscopy is utilized to diagnose the structural characteristics of the prepared silver molybdate nanostructures. The FTIR spectrum in Fig. 1b shows the stretching and bending vibrations of molecules in the silver molybdate. The peak observed at 1640, and 3569 $cm^{-1}$ were attributed to the bending and stretching vibrations of hydroxyl in the water molecules (it may be adsorbed from the atmosphere).[37,38] The bands centred at 831 and 612 $cm^{-1}$ were ascribed to the anti-symmetric Mo–O and symmetric O–Mo–O stretching vibration in $MoO_4^{2-}$ ions.[39,40] Ag–O stretching vibration of β-$Ag_2MoO_4$ could be seen at peak located at 518 $cm^{-1}$.[39]

The morphological features of the silver molybdate were investigated with the aid of transmission electron microscopy (TEM). The TEM images of the silver molybdate nanostructures

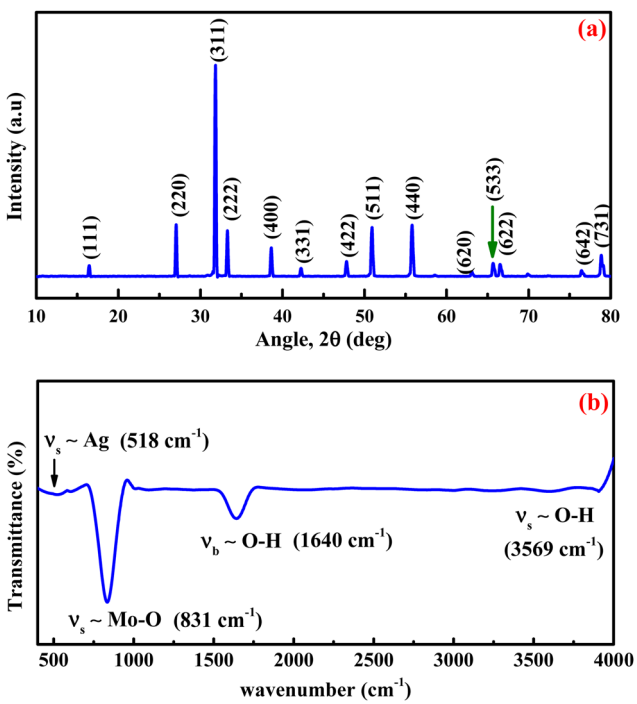


Fig. 1 (a) XRD pattern and (b) FTIR spectrum of β-$Ag_2MoO_4$ nanostructures.

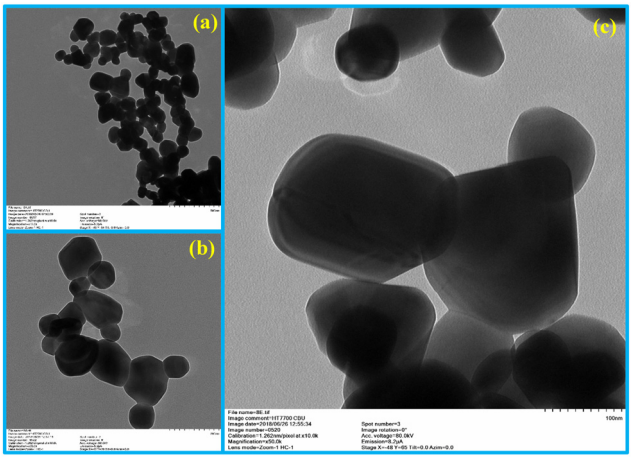


Fig. 2 TEM images of β-$Ag_2MoO_4$ under different magnification: (a) 500 nm, (b) 200 nm and (c) 100 nm.

are presented in Fig. 2, which indicates a potatoes-like structure with an average size of 121 nm. Furthermore, the image shows that the β-$Ag_2MoO_4$ nanopotatoes are interlaced, and the edges of the potatoes are visible, indicating that the β-$Ag_2MoO_4$ nanostructures are very thin. There are no aggregations observed in the TEM images, which can be ascribed to the effect of a low concentration of the precursor materials. The nanosized, aggregation-free β-$Ag_2MoO_4$ potatoes-like structures can provide effective channels for the intercalation of electrolyte ions, favouring charge storage. Hence, it can be expected to be a viable candidate for constructing supercapacitor electrodes.

It is well known that porous structures can provide a large specific surface area, allowing for excellent electrochemical performance.[41] The specific surface area and the distribution of pores with different sizes of β-$Ag_2MoO_4$ nano-potatoes were determined using BET measurements. The measurements were performed using $N_2$ adsorption and desorption isotherms and the BJH pore size distribution analysis method. Fig. 3a displays the isotherm curves of β-$Ag_2MoO_4$ nano-potatoes, demonstrating the Langmuir type IV isotherm with a characteristic H3 Hysteresis loop around the high-pressure area of 0.45 to 1.0 $P/P_0$, signifying the existence of mesopores.[41] The BET curve shown in the inset of Fig. 3a yields a specific Surface area of 34.9 $m^2\ g^{-1}$. Furthermore, the Barrett–Joyner–Halenda (BJH) approach was used to evaluate the overall distributions of pores in accordance with their sizes. Fig. 3b depicts the distribution of pores comprising various sizes in the ranges of 1.9 (12.3%), 2.1 (13.6%), 9.7 (29.9%) and 15.4 (44.2%) nm.

Herein, the major distribution of 44.2% is observed for the pore diameter of 15.4 nm, suggesting that the silver molybdate nano-potatoes are constituted with the major distribution of mesopores. Also, the pore volume of 0.12 $cm^3\ g^{-1}$ is acquired from this BJH method of analysis.

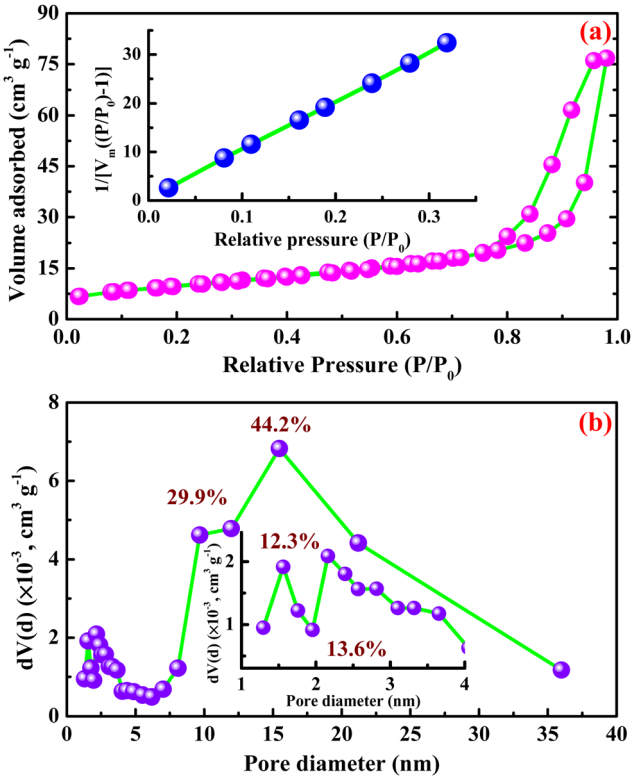


Fig. 3 (a) $N_2$ adsorption desorption isotherm curve and (b) pore size distribution curve of β-$Ag_2MoO_4$ nanostructures.

conventional heating techniques. This technique is the cost-effective and facile route to preparing uniform-sized particles. The formation of Ag–Mo–O nanostructures follows a "nucleation and growth process."[42–44] The nucleation and growth process in the formation of β-$Ag_2MoO_4$ began with mixing equal proportions of $Ag^+$ and $MoO_4^{2}$ into a blended solution. Then, the resultant solution was gradually heated to 90 °C for 10 minutes, resulting in precipitate formation (Scheme 1). When the supersaturated conditions are attained, the two $Ag^+$ ions are initially coordinated with the $MoO_4^{2-}$ ions resulting in the formation of thermodynamically stable β-$Ag_2MoO_4$.[42] Thus, the whole process is very much temperature dependent that the metal salts dissolution and β-$Ag_2MoO_4$ crystallization are accelerated by increasing the reaction temperature.[43] The plausible reactions for the formation of β-$Ag_2MoO_4$ are expressed in reactions 1 to 3:[38,44,45]

$$Na_2MoO_4 \cdot 2H_2O \xrightarrow{\text{hydrolysis}} Na^+ + MoO_4^{2-} \quad (1)$$

$$AgNO_3 \xrightarrow{\text{hydrolysis}} Ag^+ + NO_3^- \quad (2)$$

$$2Ag^+MoO_4^{2-} \xrightarrow{\text{conventional heating}} [\beta\text{-}Ag_2MoO_4]_{\text{precipitate}} \quad (3)$$

## Formation mechanism of silver molybdate nanostructures

In this work, the silver molybdate nanostructures can be said to have been prepared with energy economical, involving rapid

## Supercapacitor performance and characteristics

**Three electrode system.** The electrochemical properties of β-$Ag_2MoO_4$ were evaluated to determine its suitability as a

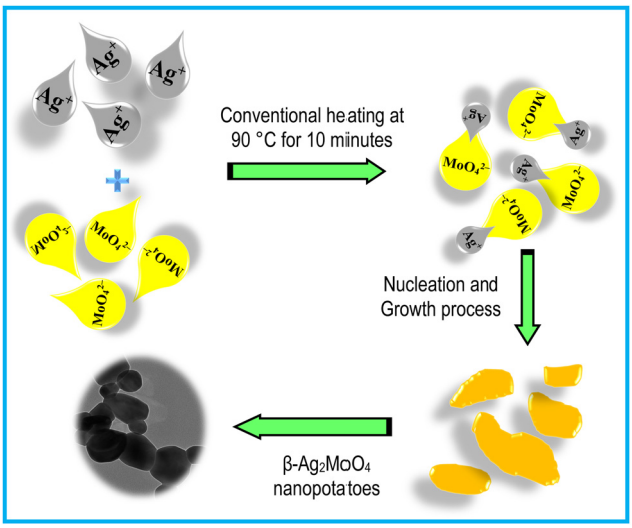


Scheme 1 Illustration of the feasible mechanism of formation of β-$Ag_2MoO_4$ nanoparticles.

positive electrode in a battery-type asymmetric supercapacitor cell (BASC) assembly. Hence, nano-potatoes of β-$Ag_2MoO_4$ electrodes were used as the working electrode in a three-electrode configuration system and examined the electrochemical behaviour in 2 M KOH electrolytes within the potential ranging from −0.45 to 0.35 V (*vs.* Ag/AgCl). The results are presented in Fig. 4. The feasible electrochemical mechanism of

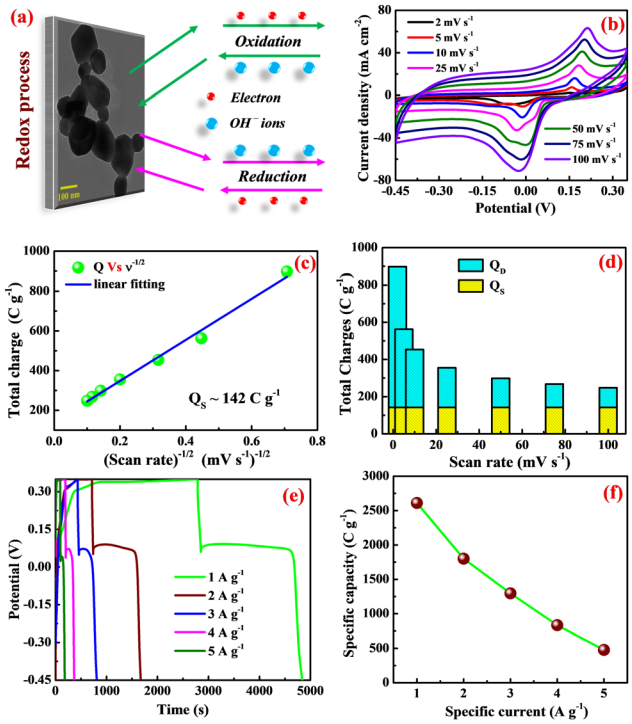


Fig. 4 Electrochemical measurements of β-$Ag_2MoO_4$: (a) redox mechanism, (b) CV curves, (c) $Q_T$ *versus* $\nu^{-1/2}$, (d) illustration of diffusion/surface charges contribution to total charges stored at various scan rates, (e) GCD curves and (f) capacity *versus* current.

β-$Ag_2MoO_4$ electrodes in an alkaline solution is demonstrated in Fig. 4a. The cyclic voltammetry measurements were initially carried out at a different scan rate of 2, 5, 10, 25, 50, 75 and 100 mV $s^{-1}$ to diagnose the nature of the energy storage mechanism in the mesoporous β-$Ag_2MoO_4$ electrodes. Fig. 4b shows the voltammograms of β-$Ag_2MoO_4$ electrodes, demonstrating the strong redox peaks at a corresponding potential. This observed behaviour suggests that the charge storage processes could be attributed to the faradaic nature, and the feasible redox reaction is: $Ag + 2OH^- \rightleftharpoons AgO + H_2O + 2e^-$ ($Ag^0$ directly oxidized to $Ag^{2+}$).[46,47] Due to the fact that the faradaic reaction includes the transfer of two electrons, there is a large area under the CV curve, which accounts for the quasi-conversion reaction mechanism. The magnitude of the anodic and cathodic current is pretty comparable (Fig. 4b), indicating that the charge storage performance is stable, and there is a complete conversion of Ag to AgO ($Ag^0 \rightarrow Ag^{2+}$) during the oxidation and *vice versa* ($Ag^{2+} \rightarrow Ag^0$) in reduction process.[46]

During the anodic current (*i.e.*, forward scan) at threshold potential, the β-$Ag_2MoO_4$ electrode is oxidized by ejecting the electron, leaving the material with unbalancing charges, corresponding to the anodic peak ($Ag^0 \rightarrow Ag^{2+}$) at a potential ranging from 150 to 210 mV for all scan rates. To maintain charge neutrality, $OH^-$ ions are diffused from the bulk electrolyte solution into the matrix of β-$Ag_2MoO_4$ electrodes. The process is reversed (*i.e.*, the reduction process) during the cathodic current (*i.e.*, reverse scan), and the cathodic peak ($Ag^{2+} \rightarrow Ag^0$) is seen at around −20 mV for all scan rates. The observation indicates that the β-$Ag_2MoO_4$ nano-potatoes electrodes are likely to be battery-type electrodes.[46] Further, a larger area under the CV curve with the increasing scan rate indicates that the electrodes of silver molybdate exhibit a high rate capability of electron discharge. The specific capacity of the potato-like β-$Ag_2MoO_4$ electrodes was estimated using the area under the CV curve (eqn (7)) and is 898, 563, 454, 356, 299, 268 and 248 C $g^{-1}$ at a scan rate of 2, 5, 10, 25, 50, 75 and 100 mV $s^{-1}$ respectively. Thus, 27.6% capacity is retained even at a high scan rate of 100 mV $s^{-1}$. This could be attributed to the low interaction of electrolyte ions with the electrochemically active sites of the β-$Ag_2MoO_4$ electrodes.

Furthermore, the electrochemical kinetics of β-$Ag_2MoO_4$ electrodes is examined using Dunn's method.[48] This method aids in distinguishing the different controlled process which is involved during charge storage performance: surface controlled (capacitive contribution; $Q_S \propto \nu$) and diffusion controlled ($Q_D \propto \nu^{-1/2}$) process. Therefore, the total quantity of charges ($Q_T$) stored in the electrochemical performance is given by:

$$Q_T = Q_S + Q_D \quad (4)$$

$$Q_T = Q_S + \text{constant}\frac{1}{\sqrt{\nu}} \quad (5)$$

Then, $Q_s$ can be estimated by plotting a graph between $Q_T$ and the inverse square root of scan rates (a linear plot; Fig. 4c). Herein, the $Q_S$ is yielded by extrapolating the linear plot and the intercept on the *y*-axis and is 142 C $g^{-1}$. Thus, the diffusion-

controlled charges ($Q_D$) are estimated by subtracting the surface-controlled charges. Fig. 4d illustrates the contribution of diffusion and surface charges to the total charge stored in the electrode. From this analysis, it is evident that the contribution of diffusion controlled process is pretty good at lower scan rates resulting in a higher specific capacity.

The charging and discharging characteristics of the potato-like β-$Ag_2MoO_4$ electrodes were examined with the galvanostatic charge–discharge test. The measurements were done at various specific currents within the potential range from −0.45 to 0.35 V. Fig. 4e depicts the non-linear charging/discharging GCD curves, evidencing that energy storage is primarily connected to the electrochemical redox process. Also, a sudden kink in discharge curves is attributed to the quasi-conversion reaction (*i.e.*, oxidation of unconverted $Ag^0$), consistent with the findings obtained in the CV analysis.[49,50] Recently, a similar charge–discharge pattern for Ag/NiO nanoparticles based on the quasi-conversion reaction has been reported elsewhere.[51] Moreover, the specific capacities (Coulombic efficiency) of 2610 (50.2%), 1800 (52.7%), 1296 (55.1%), 834 (57.2%) and 478 (69.1%) C $g^{-1}$ are estimated (using eqn (8)) at a specific current of 1, 2, 3, 4 and 5 A $g^{-1}$, respectively. These specific capacities are mainly ascribed to the unique nanosized potatoes-like structure of silver molybdate. The specific capacity is reduced at the highest tested rate of 5 A $g^{-1}$ (Fig. 2d). As the specific current increases, the electrolyte ions have less time to migrate into the matrix of silver molybdate electrodes, resulting in less dumping of charges and hence a decrease in capacity.

Furthermore, the IR drop is very small for all specific currents. For example, the GCD curve studied at 2 A $g^{-1}$ is shown in Fig. S1a (ESI†). It displays a very small amount of IR drop,[52] as seen in the enlarged graph in Fig. S1b (ESI†). The appearance of a sudden potential drop may be due to the effect of a quasi-conversion reaction (oxidation of unoxidized species during discharging). This characteristic behaviour is the inherent electrochemical nature of metallic Ag (direct oxidation from 0 to 2+ states by ejecting 2 electrons).[51]

Furthermore, the capacity of the silver molybdate nanopotatoes is higher than the recently reported values for other metal molybdate nanostructures (Table 1). The outstanding charge storage performance of $Ag_2MoO_4$ electrodes can be credited to (1) the presence of multiple valances, which enhances the electrochemical performance *via* the faradaic mechanism, (2) the formation of thin nanosized potatoes that could provide high specific surface area, enhancing the degree of accessibility of electrolyte ions, and (3) the mesoporous surface texture that facilitates the large accommodation of ions during the redox reactions.

To study the impedance characteristics associated with the diffusion of ions at the boundary between the electrode-electrolyte interface, an AC impedance analysis was performed on nano-potatoes of silver molybdate electrodes. The measurements were carried out within the frequency range of 10 mHz to 100 kHz at an amplitude of 5 mV. The Nyquist plot in Fig. 5a shows the impedance spectrum fitted to the modified Randle's circuit (inset of Fig. 5a) comprising solution resistance ($R_S$), double layer capacitance ($C_{dl}$), charge transfer resistance ($R_{CT}$), and Warburg impedance ($Z_W$), of the silver molybdate electrodes. As shown in Fig. 5a, the Nyquist plot is divided into two segments: (1) a semicircle part in the high-frequency region specifying the charge transfer controlled process and an inclined linear part in the low-frequency region, implying the dominance of the electrolyte ion diffusion process in the storage of electrical energy. Semicircles in high-frequency zones are ascribed to a combination of equivalent series resistance (ESR) and charge transfer resistance.[53] The $X$ intercept of the semicircle observed in the high-frequency region yields the electrolyte solution resistance of 1.68 Ω, and the semicircle diameter provides the charge transfer resistance of 2.95 Ω; (2) similarly, an inclined linear part in the low-frequency region, implying the dominance of the electrolyte ion diffusion process in the storage of electrical energy.

The detailed electrochemical kinetics of β-$Ag_2MoO_4$ electrode in KOH solution under ac perturbation is as follows. The results of CV and GCD provide the details of the faradaic reaction of the fabricated β-$Ag_2MoO_4$ electrode, and it indicates the diffusional transport of $OH^-$ ions onto the electrode surface. Besides, ac impedance analysis details the diffusion-

Table 1 Comparison of electrochemical characteristics of β-$Ag_2MoO_4$ with other reported metal molybdate-based nanocomposites in KOH aqueous electrolyte

| S. no. | Electrode materials | Synthesis method | Morphology | Potential window (V) | Specific capacity (C $g^{-1}$@A $g^{-1}$) | Stability (%@cycles) | Ref. |
|---|---|---|---|---|---|---|---|
| 1 | $MnMoO_4$ | Solvothermal | Nanorods | 0–0.5 | 327.4@1 | 45@1000 | 32 |
| 2 | rGO-$NiMoO_4$@Ni–Co–S | Hydrothermal | Nanotubes | 0–0.4 | 1145@1 | 88.8@10 000 | 59 |
| 3 | $CuMoO_4$/$ZnMoO_4$ | Precipitation route | Nanoflower arrays | 0–0.4 | 504@2 | 94.8@5000 | 60 |
| 4 | $ZnMoO_4$ | Hydrothermal | Interconnected nanosheets | 0–0.4 | 282@1 | 93.6@10 000 | 61 |
| 5 | $CoMoO_4$ | Hydrothermal | Spherical | 0–0.6 | 92@0.5 | — | 2 |
| 6 | $CoMoO_4$/carbon | Hydrothermal | Spherical | −0.1 to 0.42 | 851.85@1 | 86.28@3000 | 62 |
| 7 | $CuMoO_4$ | Hydrothermal | Nanosheets | −0.2 to 0.45 | 1469@1 | 90.8@5000 | 63 |
| 8 | Ag QDs/$NiMoO_4$ | Hydrothermal | Microspheres | 0–0.55 | 1141@1 | — | 64 |
| 9 | $Mn_{1/3}Ni_{1/3}Co_{1/3}MoO_4$/rGO | Hydrothermal | Nanorod bundles | 0–0.4 | 405@1 | — | 65 |
| 10 | $Ni_{0.75}Co_{0.25}MoO_4$ | Hydrothermal | Nanosheets | 0–0.55 | 400@1 | 97.2@3000 | 66 |
| 11 | $Mn_{0.33}Ni_{0.33}Co_{0.33}MoO_4$ | Hydrothermal | Nanorods | 0–0.5 | 449@2 | 83.7@2000 | 31 |
| 12 | $Mn_{0.25}Ni_{0.25}Co_{0.25}Fe_{0.25}MoO_4$ | Hydrothermal | Nanorods | 0–0.5 | 548@2 | 86.2@2000 | |
| 13 | $MoO_3$/$NiMoO_4$ | Sol–gel | Spherical nanoparticles | 0–0.6 | 122@0.5 | — | 67 |
| 14 | β-$Ag_2MoO_4$ | Conventional heating | Nanopotatoes | −0.45 to 0.35 | 2610@1 | 82@5000 | Present work |

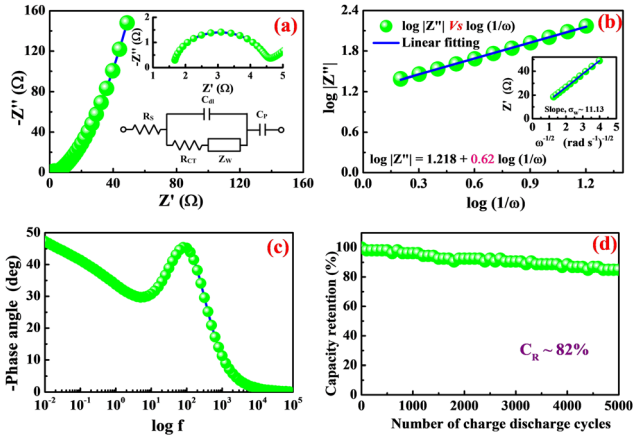


Fig. 5 (a) Nyquist plot, (b) log|$Z''$| *vs.* log(1/$\omega$), (inset of b) $Z'$ *versus* $\omega^{-1/2}$, (c) Bode phase angle plot and (d) cycle test of β-$Ag_2MoO_4$.

controlled reaction of $OH^-$ ions under ac perturbation by revealing a 45° inclined straight line in the low-frequency region. This unique electrochemical performance under ac-probing was initially suggested by Warburg and later established by Randles. Mathematically, the faradaic impedance can be expressed as the combination of charge transfer and diffusion-controlled processes ($Z_F(\omega) = R_{CT} + Z_W(\omega)$). When $\omega \rightarrow \infty$ the charge transfer is controlled, electrochemical performance is dominated by a charge-transfer controlled reaction that dominates the charge storage process. The semicircle in the high-frequency region of the Nyquist plot addresses the charge transfer controlled reaction. Similarly, the diffusion-controlled electrochemical behaviour has been observed when $\omega$ of ac probe undergoes to 0 ($\omega \rightarrow 0$), and it corresponds to the straight line (45° inclination to $Z'$) in the low-frequency region. Mathematically, it can be expressed as[1]

$$Z_W(\omega) = \frac{\sigma}{\omega^{\alpha}}(1 - j) \quad \text{or} \quad \log|Z''| = \log\sigma + \alpha\log\left(\frac{1}{\omega}\right);$$

where $\sigma$ is the Warburg coefficient, $j$ is an imaginary unit, $\omega$ stands for angular frequency (rad $s^{-1}$), and $\alpha$ corresponds to the transfer coefficient, and it can be obtained from the slope of the linear plot between log|$Z''$| and log(1/$\omega$) that indicates the nature of the electrochemical performance of the electrode materials ($\alpha$ takes 0.5 for the Warburg behaviour).[54,55]

Fig. 5b displays the linear plot of log|$Z''$| *versus* log(1/$\omega$) of β-$Ag_2MoO_4$. Furthermore, the slop of 0.62 is obtained for the straight line, corresponding to the transfer coefficient ($\alpha$) reflecting Warburg behaviour. The transfer coefficient value is nearer to 0.5, indicating diffusion-controlled energy storage performance, supporting the result obtained from the cyclic voltammetry technique (*i.e.* diffusion-controlled process). Moreover, the hydroxyl ion diffusion coefficient is estimated using the relation 6.[55]

$$D = \frac{R^2T^2}{2A^2n^4F^4C^2\sigma_W^2} \quad (6)$$

where $R$, gas constant (8.314 J $mol^{-1}$ $K^{-1}$); $T$, temperature (room temperature usually taken as 295 K), $A$, surface area (1 $cm^2$); $n$, number of electrons transferred (2); $F$, Faraday constant (96 485 C $mol^{-1}$); $C$, the molar concentration of $OH^-$ ions (2 × $10^{-3}$ mol $cm^{-3}$ for three-electrode and 6 × $10^{-3}$ mol $cm^{-3}$ for two-electrode) and $\sigma_W$, Warburg coefficient (11.13); this value is obtained from the slope of $Z'$ *versus* $\omega^{-1/2}$ linear plot, which is shown in the inset of Fig. 5b. The estimated diffusion coefficient is 30.42 × $10^{-15}$ $cm^2$ $s^{-1}$. The Bode phase angle plot of β-$Ag_2MoO_4$ is displayed in Fig. 5c. In the phase angle plot, the approaching to pure capacitive behaviour at low frequency is usually identified with the phase angle approaching −90°. Whereas, the Bode phase angle plot of β-$Ag_2MoO_4$ intercepts at a low frequency around a phase angle of −45° suggesting an excellent redox performance. The smaller the phase angle, the better the charge storage performance and the faster the diffusion of the ions.[56,57] Furthermore, the Bode phase angle plot demonstrates one time constant at the middle frequency region, signifying the double layer capacitance process.[58] Thus, the result obtained in the Bode phase angle analysis over frequency is consistent with the results obtained in Dunn's method (surface contribution of 142 C $g^{-1}$).

Besides, the nano-potatoes of β-$Ag_2MoO_4$ electrode were further employed to investigate the cycle life test. The measurements were performed through the GCD technique at a specific current of 10 A $g^{-1}$ for 5000 continuous GCD cycles, and the results are displayed in Fig. 5d. faradaic efficiency and capacity retention are studied in the cycle life test.[41] The electrodes of β-$Ag_2MoO_4$ nano-potatoes could yield an average faradaic efficiency of 97% for over 5000 continuous charge–discharge cycles. Also, capacity retention is estimated at an interval of 100 GCD cycles. The electrodes of β-$Ag_2MoO_4$ nano-potatoes displayed decreasing trendy capacity from its initial value and retained 82% of its initial value even after 5000 charge–discharge cycles. The combined effect of nanosized potato structure and mesoporous texture is primarily responsible for the remarkable electrochemical performance. To better understand the sustainability of the β-$Ag_2MoO_4$ electrodes, we have recorded SEM images after the cycling stability test and presented them in Fig. S2 (ESI†). It indicates that the β-$Ag_2MoO_4$ lost its morphology and showed the aggregation of particles, and the closure of electroactive sites led to the capacity fading.

**Two electrode system.** The real-life application of the prepared β-$Ag_2MoO_4$ nano-potatoes electrodes was tested in an asymmetric supercapacitor device (Fig. 6a). In this device assembly, the β-$Ag_2MoO_4$ is the positive electrode, and activated carbon is employed as the counter electrode to the β-$Ag_2MoO_4$. The charge conservation is the key route to obtaining superior charge storage performance, and it can be achieved through the mass balance theory.[50] The CV curves, studied at 50 mV $s^{-1}$, of the β-$Ag_2MoO_4$ (−0.45 to 0.35 V) and AC (−1 to 0 V) electrodes are presented in Fig. 6b. The mass ratio is assessed by taking into account the specific capacity of 299 C $g^{-1}$ (β-$Ag_2MoO_4$) and 526 C $g^{-1}$ (AC) at a scan rate of 50 mV $s^{-1}$ in eqn (9), and it is 2.2. (*i.e.*, $m_+ = m_- \times 2.2$).[50] The total mass ($m_+ + m_-$) of the active material used to assemble is 4.8 mg.

The charge storage performance of the battery-type asymmetric supercapacitor cell operated at 1.5 V is shown in

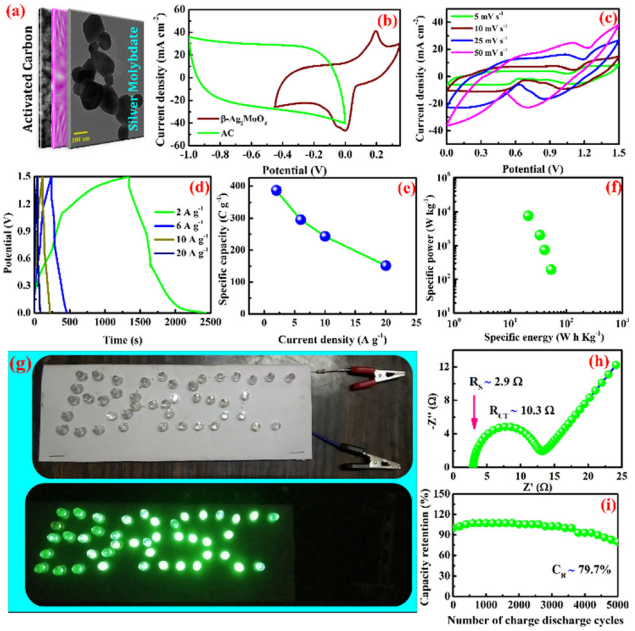


Fig. 6 (a) Schematic representation of BASCs, (b) CV curves of AC (−1 to 0 V) and β-$Ag_2MoO_4$ (−0.45 to 0.35 V), supercapacitor performance of cell: (c) CV curves, (d) GCD curves, (e) $C_S$ *vs.* $I_D$, (f) Ragone plot, (g) charged cell is energizing the green LEDs, (h) Nyquist plot and (i) cyclic stability.

Fig. 6c–i. The CV curves (Fig. 6c) of the cell demonstrate the non-capacitive faradaic energy storage process by displaying non-ideal rectangular shape voltammograms.

Fig. 6d shows GCD curves of the asymmetric supercapacitor cell that confirms the electrochemical performance *via* the faradaic process. The specific capacity of the asymmetric supercapacitor cell is estimated using the area of the discharge curve, and the values are 392, 297, 262 and 101 C $g^{-1}$ at the constant specific currents of 2, 6, 10 and 20 A $g^{-1}$ respectively (Fig. 6e).[68] It is interesting to note that this device holds the capacity of 101 C $g^{-1}$ at a higher current rate of 20 A $g^{-1}$ indicates the batter rate capacity of the device. Further, the specific energy and power are estimated using eqn (10) and (11), and the values are presented in a Ragone plot (Fig. 6f).[68] The estimated specific energies are 54, 41, 34 and 21 W h $kg^{-1}$ at a delivery rate of 194, 739, 2029 and 7582 W $kg^{-1}$, respectively. Even at a higher power of 7582 W $kg^{-1}$, about 38.8% energy is retained, reflecting a superior electrochemical response of the BASC.

Moreover, the charged cell (4 Nos; connected in series) could energize the LEDs (connected in parallel), as shown in Fig. 6g. Therefore, the specific energy estimated for the β-$Ag_2MoO_4$//AC battery-type Asymmetric supercapacitor cell (BASC) could be comparable with the previously reported cell (Table 2). The solution ($R_S$) and charge transfer resistance ($R_{CT}$) of 2.9 Ω and 10.3 Ω were obtained from the *X* intercept and diameter of the semicircle (Fig. 6h, Nyquist plot, fitted to the modified Randle's circuit), respectively. The lifespan of the hybrid-type β-$Ag_2MoO_4$//AC cell upon 5000 continuous GCD cycles is examined using galvanostatic charge/discharge analysis at a current density of 15 mA $cm^{-2}$. Faradaic efficiency and capacity retention are assessed for each interval of 200 cycles, and they are presented in Fig. 6i.[41] The hybrid pseudocapacitor cell could retain 79.7% of specific capacity from its initial value even after 5000 continuous charge–discharge cycles. Furthermore, the hybrid cell yields an average faradaic efficiency of 91.2% up to 5000th charge–discharge cycles.

## Conclusion

In summary, a facile energy economic aqueous precipitation route of fabricating the mesoporous textured β-$Ag_2MoO_4$ nano-potatoes was developed in this research work. The nanosized potatoes have a remarkable charge storage performance by estimating a maximum specific capacity of 2160 C $g^{-1}$ (1 A $g^{-1}$) and 82% retention (5000 cycles). Such superior charge storage performance arises out of the rapid faradaic reaction kinetics across the electrode and electrolyte interface along with quasi-conversion reaction. The designed β-$Ag_2MoO_4$//AC redox-type asymmetric supercapacitor cell could yield 38.8% retention in specific energy even at a higher specific power of 7.6 kW $kg^{-1}$ and better stability (79.7% retention after 5000 cycles). This article illustrates a framework for making mesoporous structures using noble metal for supercapacitor applications.

## Experimental

### Chemicals and reagents

Silver nitrate ($AgNO_3$, Sigma-Aldrich, AR), sodium molybdate ($Na_2MoO_4{\cdot}2H_2O$, Sigma-Aldrich, 99%), and all other chemicals

Table 2 Comparison of electrochemical performance of β-$Ag_2MoO_4$//AC supercapacitor cell with previously reported metal molybdate-based asymmetric supercapacitor cell

| S. no. | Asymmetric supercapacitor cells | Potential window (V) | Separator/electrolyte | $E_S$ (W h $kg^{-1}$) | $P_S$ (W $kg^{-1}$) | Stability | Ref. |
|---|---|---|---|---|---|---|---|
| 1 | $CoMoO_4/Co_{1-x}S$//AC | 1.6 | — | 39.8 | 804.5 | 86.4@5000 | 69 |
| 2 | $CuCo_2S_4$@$CoMoO_4$//AC | 1.4 | — | 45.73 | 198.8 | 83@3000 | 70 |
| 3 | $NiCo_2S_4$@$NiMoO_4$//AC | 1.6 | Cellulose separator | 53.2 | 560 | 90.2@8000 | 71 |
| 4 | rGO-NMO@NCS//rGO-MDC | 1.6 | — | 57.24 | 801.8 | 92.42@6000 | 59 |
| 5 | $CuMoO_4/ZnMoO_4$//AC | 1.5 | Filter paper | 34.83 | 472.0 | 89.6@8000 | 60 |
| 6 | CMO-GC-2//AC | 1.5 | Polypropylene film | 36.86 | 152.84 | 87@5000 | 62 |
| 7 | Ag-QDs/$NiMoO_4$//AC | 1.7 | Cellulose separator | 48.5 | 212.5 | 84.4@5000 | 64 |
| 8 | $Cu_3Mo_2O_9$//$La_2Mo_3O_{12}$ | 1.6 | — | 21.84 | 1610 | 119.4@5000 | 72 |
| 9 | Co-$NiMoO_4$//AC | 1.6 | Cellulose separator | 31.1 | 1249.9 | 91@5000 | 73 |
| 10 | β-$Ag_2MoO_4$//AC | 1.5 | Polyurethane foam | 54 | 194 | 79.7@5000 | Present work |

were obtained from CDH chemical company and used for material preparation as supplied with no further purification. All chemicals were reagent grade.

### Preparation of silver molybdate nanostructures

The silver molybdate nanostructures were prepared through a rapid wet chemical route, which required using a concentration ratio of 1 : 1 of Ag to Mo (*i.e.*, containing 1 mM of each metal ion) in the initial solution. In detail, 241.6 mg of $Na_2MoO_4 \cdot 2H_2O$ was dissolved in 50 ml of double-distilled water and stirred for 30 minutes to ensure homogeneity. Similarly, the Ag-containing solution was prepared by dissolving 339.65 mg of $AgNO_3$ in 50 ml of double-distilled water and stirred for 30 minutes. Then, the $AgNO_3$ and $Na_2MoO_4$ solutions were gradually added to each other. The blended solution was continuously stirred for 1 hour. The resultant solution mixture (with 1 mM of $Na_2MoO_4$ and $AgNO_3$) was heated to 90 °C for 10 minutes until a precipitate formed. The obtained precipitate is washed 5 times with double distilled water to remove the residues of reaction and then dried at 80 °C for 24 hours in an atmosphere of air.

### Electrode preparation and characterization

The crystal phase and structure of the prepared silver molybdate materials were analyzed using XRD (Rigaku Miniflux 600 X-Ray Diffractometer, CuKα radiation, $\lambda$ = 0.1452 nm, 40 kV, 15 mA). Their morphology was investigated using a transmission electron microscope (JEOL/JEM 2100, LaB6 source, 200 kV). The specific surface area was determined using $N_2$ adsorption and desorption with Brunauer–Emmett–Teller (BET) equation (Nova Station 0, Quantachrome Instruments, version 3.0) and porosity with Barrett–Joyner–Halenda method.

The electrochemical performance of the silver molybdate electrodes was determined using three-electrode electrochemical cells (Electrochemical Workstation, CHI 660C; 5.01 revised 1/5/2007). The preparation of electroactive material and working electrodes have been discussed in the S3 (ESI†).[41] The preparation of electroactive material, and working electrodes have been reported elsewhere.[41] Ag/AgCl electrodes and platinum wire were used as reference and counter electrodes, respectively. Electroanalytical techniques like cyclic voltammetry (CV), galvanostatic charge–discharge (GCD) and electrochemical impedance spectroscopy (EIS) were adopted to investigate the supercapacitive behaviour of the prepared material in 2 M KOH solutions. The specific capacity of the silver molybdate electrodes was estimated from the CV and GCD test with the following eqn (8) and (9), respectively,[50,68,74]

$$Q_s = \frac{\int I \mathrm{d}V}{2 m_{el} v} \quad (7)$$

$$Q_s = \frac{2 I \int V \mathrm{d}t}{m_{el} V} \quad (8)$$

where $Q_S$ is the specific capacity (C $g^{-1}$); $\int I \mathrm{d}V$ is the area under the CV curve (A V); $m_{el}$ is the mass of the electroactive material loaded (g); $V$, potential window (V); $\nu$, scan rate (mV $s^{-1}$); $I$, specific current (A $g^{-1}$) and $\int V \mathrm{d}t$, area of the discharge curve (V s).

### Design of assembly β-$Ag_2MoO_4$//AC battery-type asymmetric supercapacitor cell (BASC)

The battery-type asymmetric supercapacitor cell (BASC) was designed in a sandwich model. The silver molybdate was placed as the positive electrode, activated carbon as the counter electrode, and polyurethane foam soaked in 6 M KOH (due to the starvation of electrolyte ions in 2 M KOH)[75,76] was the separator-cum-charge reservoir. Crucial to an outstanding charge storage performance is balancing the charges ($Q^+ = Q^-$) produced at the surface of activated carbon and silver molybdate electrodes, which can be done through mass balance theory ($Q = mCV$; eqn (10)).[77,78]

$$\frac{m_+}{m_-} = \frac{C_- V_-}{C_+ V_+} = \frac{Q_-}{Q_+} \quad (9)$$

where $m_+$ and $m_-$ are masses (g); $Q_+$ and $Q_-$ are specific capacities (C $g^{-1}$) of the activated carbon and silver molybdate electrodes, respectively. Then, the specific energy and power were estimated using the following equations.[50,68,74]

$$E_S = \frac{I \int V(t) \mathrm{d}t}{m_{ele} 3.6} \quad (10)$$

$$P_S = \frac{E_S}{t} \times 3600 \quad (11)$$

where $E_S$ – specific energy (W h $kg^{-1}$); $I$ – applied current (A); $\int V(t) \mathrm{d}t$ – area (excluding the discharge area of bare Ni foam) under discharge curve (V s); $m_{ele}$ is the mass of active material loaded (g); PS is the specific power (W $kg^{-1}$), and $t$ is discharge time (s).

## Conflicts of interest

There are no conflicts to declare.

## Acknowledgements

This work was done within a collaboration agreement between Cape Breton University, Nova Scotia, Canada and Dr Mahalingam College of Engineering and Technology (MCET), Tamil Nadu, India. The authors acknowledge the support from Nachimuthu Industrial Association and its Secretary, Dr C. Ramaswamy. The work partially benefitted from funding through the CBU's RISE Grant Program, NSERC Discovery Grant to MM, CFI, NSRIT, MITACS, and Research Nova Scotia grants.

## Notes and references

1 A. Muzaffar and M. Ahamed, *Ceram. Int.*, 2019, **45**, 4009–4015.
2 I. Shaheen, K. S. Ahmad, C. Zequine, R. K. Gupta, A. Thomas and M. A. Malik, *RSC Adv.*, 2020, **10**, 8115–8129.

3 M. Kandasamy, S. Sahoo, S. K. Nayak, B. Chakraborty and C. S. Rout, *J. Mater. Chem. A*, 2021, **9**, 17643–17700.
4 J. Li, C. Zhao, Y. Yang, C. Li, T. Hollenkamp, N. Burke, Z. Y. Hu, G. Van Tendeloo and W. Chen, *J. Alloys Compd.*, 2019, **810**, 151841.
5 H. Deng, J. Huang, Z. Hu, X. Chen, D. Huang and T. Jin, *ACS Omega*, 2021, **6**, 9426–9432.
6 J. Acharya, B. Pant, G. Prasad Ojha and M. Park, *J. Colloid Interface Sci.*, 2022, **610**, 863–878.
7 D. Zhu, X. Sun, J. Yu, Q. Liu, J. Liu, R. Chen, H. Zhang, D. Song, R. Li and J. Wang, *J. Colloid Interface Sci.*, 2020, **574**, 355–363.
8 R. Liang, Y. Du, J. Wu, X. Li, T. Liang, J. Yuan, P. Xiao and J. Chen, *J. Solid State Chem.*, 2022, **307**, 122845.
9 Y. Wang, S. Yu, C. Y. Deng, H. L. Wei, J. H. Zhou, Z. X. Chen, H. Yang, M. J. Liu, B. N. Gu, C. C. Chung, H. F. Lv, Z. Y. Zhou and Y. L. Chueh, *ACS Appl. Mater. Interfaces*, 2022, **14**, 8282–8296.
10 V. Kumar, S. Matz, D. Hoogestraat, V. Bhavanasi, K. Parida, K. Al-Shamery and P. S. Lee, *Adv. Mater.*, 2016, **28**, 6966–6975.
11 L. Zhang, S. Zheng, L. Wang, H. Tang, H. Xue and G. Wang, *Small*, 2017, **13**, 1700917.
12 Z. Zhu, Y. Sun, C. Li, C. Yang, L. Li, J. Zhu, S. Chou, M. Wang, D. Wang and Y. Li, *Mater. Chem. Front.*, 2021, **5**, 7403–7418.
13 T. Yan, M. Wang, K. Li, X. Ni, X. Du, M. Xi, H. Chen and A. Ju, *J. Alloys Compd.*, 2022, **898**, 162834.
14 F. N. I. Sari and J. Ting, *ChemSusChem*, 2018, **11**, 897.
15 X. Tian, T. Yang, Y. Song, Y. Li, H. Peng, R. Xue, X. Ren and Z. Liu, *J. Energy Storage*, 2022, **47**, 1–8.
16 A. S. Keshari and P. Dubey, *Dalton Trans.*, 2022, **51**, 3992–4009.
17 S. Liu, Y. Yin, D. Ni, K. S. Hui, K. N. Hui, S. Lee, C. Y. Ouyang and S. C. Jun, *Energy Storage Mater.*, 2019, **19**, 186–196.
18 Q. Li, Y. Li, J. Zhao, S. Zhao, J. Zhou, C. Chen, K. Tao, R. Liu and L. Han, *J. Power Sources*, 2019, **430**, 51–59.
19 M. W. Ahmad, S. Anand, K. Shalini, M. Ul-Islam, D. J. Yang and A. Choudhury, *Mater. Sci. Semicond. Process.*, 2021, **136**, 106176.
20 R. Sheng, J. Hu, X. Lu, W. Jia, J. Xie and Y. Cao, *Ceram. Int.*, 2021, **47**, 16316–16323.
21 H. W. Nam, C. V. V. M. Gopi, S. Sambasivam, R. Vinodh, K. V. G. Raghavendra, H. J. Kim, I. M. Obaidat and S. Kim, *J. Energy Storage*, 2020, **27**, 101055.
22 X. Xu, C. Zhao, X. Liu, Y. Liu, P. Dong and C. Itani, *J. Mater. Sci.: Mater. Electron.*, 2020, **31**, 3631–3641.
23 P. Li, C. Ruan, J. Xu and Y. Xie, *Nanoscale*, 2019, **11**, 13639–13649.
24 U. T. Nakate, P. Patil, Y. T. Nakate, S. I. Na, Y. T. Yu and Y. B. Hahn, *Appl. Surf. Sci.*, 2021, **551**, 149422.
25 B. Saravanakumar, G. Ravi, R. Yuvakkumar, V. Ganesh and R. K. Guduru, *Mater. Sci. Semicond. Process.*, 2019, **93**, 164–172.
26 G. Nagaraju, S. Chandra Sekhar, B. Ramulu and J. S. Yu, *Appl. Surf. Sci.*, 2019, **471**, 795–802.
27 C. Wang, D. Wu, Y. Qin and Y. Kong, *Chem. Commun.*, 2021, **57**, 4019–4022.
28 I. Hussain, A. Ali, C. Lamiel, S. G. Mohamed, S. Sahoo and J. J. Shim, *Dalton Trans.*, 2019, **48**, 3853–3861.
29 I. Shaheen, K. S. Ahmad, C. Zequine, R. K. Gupta, A. G. Thomas and M. A. Malik, *J. Mater. Sci.*, 2020, **55**, 7743–7759.
30 Z. Yu, N. Zhang, G. Li, L. Ma, T. Li, Z. Tong, Y. Li and K. Wang, *J. Energy Storage*, 2022, **51**, 104511.
31 A. B. Appiagyei and J. I. Han, *Ceram. Int.*, 2020, **46**, 12422–12429.
32 B. Saravanakumar, S. P. Ramachandran, G. Ravi, V. Ganesh, A. Sakunthala and R. Yuvakkumar, *Appl. Phys. A: Mater. Sci. Process.*, 2019, **125**, 1–11.
33 J. Yesuraj, S. Austin Suthanthiraraj and O. Padmaraj, *Mater. Sci. Semicond. Process.*, 2019, **90**, 225–235.
34 D. Combs, B. Godsel, J. Pohlman-Zordan, A. Huff, J. King, R. Richter and P. F. Smith, *RSC Adv.*, 2021, **11**, 39523–39533.
35 P. B. Almeida, I. M. Pinatti, R. C. de Oliveira, M. M. Teixeira, C. C. Santos, T. R. Machado, E. Longo and I. L. V. Rosa, *Chem. Pap.*, 2021, **75**, 1869–1882.
36 A. Zareie-Darmian, H. Farsi, A. Farrokhi, R. Sarhaddi and Z. Li, *Phys. Chem. Chem. Phys.*, 2021, **23**, 9539–9552.
37 S. K. Gupta, P. S. Gosh, K. Sudarshan, R. Gupta, P. Pujari and R. M. Kadam, *Dalton Trans.*, 2015, **44**, 19097–19110.
38 M. Abinaya, R. Rajakumaran, S. M. Chen, R. Karthik and V. Muthuraj, *ACS Appl. Mater. Interfaces*, 2019, **11**, 38321–38335.
39 J. V. Kumar, R. Karthik, S. Chen, V. Muthuraj and C. Karuppiah, *Sci. Rep.*, 2016, **6**, 1–13.
40 T. Cheng, H. Gao, X. Sun, T. Xian, S. Wang, Z. Yi, G. Liu, X. Wang and H. Yang, *Adv. Powder Technol.*, 2021, **32**, 951–962.
41 J. J. William, I. M. Babu and G. Muralidharan, *Mater. Chem. Phys.*, 2019, **224**, 357–368.
42 C. Ponzoni, R. Rosa, M. Cannio, V. Buscaglia, E. Finocchio, P. Nanni and C. Leonelli, *J. Alloys Compd.*, 2013, **558**, 150–159.
43 S. H. Han, K. S. Kim, H. G. Kim, H. G. Lee, H. W. Kang, J. S. Kim and C. Il Cheon, *Ceram. Int.*, 2010, **36**, 1365–1372.
44 P. Xiao, L. Zhu, Y. Zhu and Y. Qian, *J. Solid State Chem.*, 2011, **184**, 1459–1464.
45 A. F. Gouveia, J. C. Sczancoski, M. M. Ferrer, A. S. Lima, M. R. M. C. Santos, M. S. Li, R. S. Santos, E. Longo and L. S. Cavalcante, *Inorg. Chem.*, 2014, **53**, 5589–5599.
46 A. C. Lokhande, P. T. Babar, V. C. Karade, J. S. Jang, V. C. Lokhande, D. J. Lee, I. C. Kim, S. P. Patole, I. A. Qattan, C. D. Lokhande and J. H. Kim, *Mater. Today Chem.*, 2019, **14**, 100181.
47 M. B. Poudel, H. P. Karki and H. J. Kim, *J. Energy Storage*, 2020, **32**, 101693.
48 I. M. Babu, J. J. William and G. Muralidharan, *Appl. Surf. Sci.*, 2019, **480**, 371–383.
49 S. X. Wang, C. C. Jin and W. J. Qian, *J. Alloys Compd.*, 2014, **615**, 12–17.
50 J. Johnson William, I. Manohara Babu and G. Muralidharan, *Chem. Eng. J.*, 2021, **422**, 130058.
51 S. Nagamuthu and K.-S. Ryu, *Sci. Rep.*, 2019, **9**, 4864.

 

52 N. Devillers, S. Jemei, M. Péra, D. Bienaimé and F. Gustin, *J. Power Sources*, 2014, **246**, 596–608.
53 K. K. Purushothaman, I. M. Babu and B. Saravanakumar, *Int. J. Hydrogen Energy*, 2017, **42**, 28445–28452.
54 S. Sarker, A. J. S. Ahammad, H. W. Seo and D. M. Kim, *Int. J. Photoenergy*, 2014, 1–17.
55 J. J. William, I. M. Babu and G. Muralidharan, *New J. Chem.*, 2019, **43**, 15375–15388.
56 D. Malko, T. Lopes, E. A. Ticianelli and A. Kucernak, *J. Power Sources*, 2020, **323**, 189–200.
57 W. Kang, X. Kong, J. Li, P. Wang, Y. Sun, X. Zhang, H. Yang and B. Lin, *Mater. Today Energy*, 2020, **18**, 100549.
58 L. Wang, X. Zhang, Y. Yin, D. Trans and D. O. I. Cdte, *Dalton Trans.*, 2017, **46**, 10545–10548.
59 J. Acharya, G. P. Ojha, B. S. Kim, B. Pant and M. Park, *ACS Appl. Mater. Interfaces*, 2021, **13**, 17487–17500.
60 A. B. Appiagyei, J. O. Bonsu and J. I. Han, *J. Mater. Sci.: Mater. Electron.*, 2021, **32**, 6668–6681.
61 Y. P. Gao, K. J. Huang, C. X. Zhang, S. S. Song and X. Wu, *J. Alloys Compd.*, 2018, **731**, 1151–1158.
62 R. M. Bhattarai, S. Moopri Singer Pandiyarajan, S. Saud, S. J. Kim and Y. S. Mok, *Dalton Trans.*, 2020, **49**, 14506–14519.
63 M. Farahpour and M. Arvand, *J. Energy Storage*, 2021, **40**, 102742.
64 X. Zhang, Z. Li, Z. Yu, L. Wei and X. Guo, *Appl. Surf. Sci.*, 2020, **505**, 144513.
65 S. Jayasubramaniyan, S. Balasundari, N. Naresh, P. A. Rayjada, S. Ghosh, N. Satyanarayana and P. Muralidharan, *J. Alloys Compd.*, 2019, **778**, 900–912.
66 P. Sun, C. Wang, W. He, P. Hou and X. Xu, *ACS Sustainable Chem. Eng.*, 2017, **5**, 10139–10147.
67 I. Shaheen, K. S. Ahmad, C. Zequine, R. K. Gupta, A. G. Thomas and M. A. Malik, *J. Energy Storage*, 2020, **29**, 101309.
68 A. Laheäär, P. Przygocki, Q. Abbas and F. Béguin, *Electrochem. Commun.*, 2015, **60**, 21–25.
69 J. Ge, J. Wu, L. Fan, Q. Bao, J. Dong, J. Jia, Y. Guo and J. Lin, *J. Energy Chem.*, 2018, **27**, 478–485.
70 X. Mao, Y. Wang, C. Xiang, D. Zhan, H. Zhang, E. Yan, F. Xu, X. Hu, J. Zhang, L. Sun and Y. Zou, *J. Alloys Compd.*, 2020, **844**, 156133.
71 S. Chen, Z. Zhang, W. Zeng, J. Chen and L. Deng, *ChemElectroChem*, 2019, **6**, 590–597.
72 V. Gajraj and C. R. Mariappan, *Appl. Surf. Sci.*, 2020, **512**, 145648.
73 Y. Meng, D. Yu, J. Liu, C. Guo, Y. Hua, C. Wang, X. Zhao and X. Liu, *J. Alloys Compd.*, 2021, **884**, 161092.
74 J. J. William, I. M. Babu and G. Muralidharan, *New J. Chem.*, 2019, **43**, 15375–15388.
75 S. G. Kandalkar, J. L. Gunjakar and C. D. Lokhande, *Appl. Surf. Sci.*, 2008, **254**, 5540–5544.
76 I. M. Babu, J. J. William and G. Muralidharan, *J. Solid State Electrochem.*, 2019, **23**, 1325–1338.
77 Y. Liu, X. Cao, L. Cui, Y. Zhong, R. Zheng, D. Wei, C. Barrow, J. M. Razal, W. Yang and J. Liu, *J. Power Sources*, 2019, **437**, 226897.
78 B. Huang, D. Yao, J. Yuan, Y. Tao, Y. Yin, G. He and H. Chen, *J. Colloid Interface Sci.*, 2022, **606**, 1652–1661.